Nuclear Materials and Energy 15 (2018) 237–243

Contents lists available at ScienceDirect

Nuclear Materials and Energy

journal homepage: www.elsevier.com/locate/nme

Investigation of precipitate in an austenitic ODS steel containing a carbon-rich process control agent

Tim Gräning[a,*], Michael Rieth[a], Anton Möslang[a], Alexei Kuzmin[b], Andris Anspoks[b], Janis Timoshenko[b], Arturs Cintins[b], Juris Purans[b]

[a] Institute for Applied Materials (IAM), Karlsruhe Institute of Technology (KIT), Hermann-von-Helmholtz-Platz 1, Eggenstein Leopoldshafen 76344, Germany
[b] Institute of Solid State Physics, University of Latvia, Kengaraga street 8, Riga LV-1063, Latvia

ARTICLE INFO

Keywords:
Oxide dispersion strengthened steel
Mechanical alloying
Austenitic steel
Process control agent
Transmission electron microscopy
X-ray absorption spectroscopy

ABSTRACT

Austenitic oxide dispersion strengthened (ODS) steels are one of the candidates as a structural material for high-temperature applications in future power plants. To guarantee the necessary high production yield, the production process was improved in terms of reproducibility and scalability, by adding a process control agent (PCA) during the milling process. Due to this addition and the inherent change of the production process, the produced powder was thoroughly investigated using transmission electron microscopy and X-ray absorption spectroscopy methods to reveal the formation of chromium-rich carbides adjunct to titanium. Hence, less titanium was available to form the preferred complex nano-oxides the addition of carbon to the system influences the formation of precipitates severely in terms of their amount and size. The mechanical alloying process itself was unaffected by the addition of a PCA, and mixing and alloying of used elements still occurs.

1. Introduction

Ferritic oxide dispersion strengthened (ODS) steels have been developed as a possible material for structural applications in future fusion power plants [1–7]. Due to the inferior behavior under irradiation, austenitic steels were disregarded for applications which expose the material to such conditions. However, in recent years the interest in austenitic ODS steels was reignited, due to its corrosion resistance, the high-temperature stability of the microstructure, and an exhibited high ductility in a tensile test at 700 °C [8–12].

Nevertheless, problems with the adhesion of ductile austenitic powder in a high energy Simoloyer mill lead to a severely decreased powder production yield [13]. Preliminary in-house tests have shown that an added process control agent (PCA) helps to keep the powder production yield at 100% during mechanical alloying by reducing the adhesion of the powder to other components inside the mill while using a novel two-step milling process, described elsewhere [14]. However, the addition of a carbon-containing PCA changes the milling process and adds carbon as an element to the process [15]. This paper focuses on the investigation of the impact of carbon on the microstructure and the formation of nanoparticles inside the powder particles. Powder particles after the first and second milling step were examined to gain insights about the formed microstructure after the mechanical alloying process was finished. A subsequent heat treatment of powder particles was applied to initiate the formation of precipitates, followed by an examination of the microstructure using transmission electron microscopy (TEM) and X-ray absorption spectroscopy (XAS) as complementary methods to determine the effect of carbon on the formation and stability of ODS particles in mechanically alloyed powder. In addition, this study is performed to provide a baseline for understanding the influences of a subsequent extrusion process and a long-term annealing on the microstructure and formation of precipitates.

2. Materials and methods

A novel two-step mechanical alloying process was conducted to produce an austenitic ODS steel powder [14]. The first step consisted of blending a ferritic base powder, labeled as PCA-0, with Fe_3Y and elemental chromium powder followed by mechanical alloying in a Simoloyer mill for 40 h. This way, a ferritic ODS powder was produced, hereinafter referred to as PCA-1. This powder was then mixed and mechanically alloyed with elemental nickel powder and stearic acid. Stearic acid was added as a carbon-containing PCA to reduce the adhesion of nickel and of the formed austenitic powder particles to the milling container. Thus, this addition enables a powder production yield of 100% in the second milling step. The duration of the second milling step was between 10 and 12 h, and the attained powder is hereinafter termed as PCA-2. To investigate the precipitate formation

* Corresponding author.
E-mail address: tim.graening@kit.edu (T. Gräning).

https://doi.org/10.1016/j.nme.2018.05.005
Received 7 December 2017; Received in revised form 11 April 2018; Accepted 8 May 2018
Available online 24 May 2018

Table 1
Powders used for milling.

Powder	Comments	Average particle size / μm	Milling time/ hours
PCA-0	Base Alloy	140	–
PCA-1	PCA-0 + Fe_3Y + Cr	undefined	40
PCA-2	PCA-1 + Ni + stearic acid	undefined	10–12
Fe_3Y	Added before 1st milling step	400	–
Cr	Added before 1st milling step	250	–
Ni	Added before 2nd milling step	5	–
Stearic acid	Added before 2nd milling step	10	–

and thermal stability of the microstructure, the powder PCA-2 was annealed at 1100 °C for 40 h. In comparison, non-annealed powders of PCA-1 and PCA-2 were investigated to examine the homogeneity and distribution of elements. Specifications of the used powders are summarized in Table 1 and Table 2 provides information of the determined chemical composition. The amount of oxygen was identified applying a carrier gas hot extraction method, while carbon was determined using a carbon/ sulfur analyzer. Inductively coupled plasma optical emission spectrometry (ICP-OES) was applied for all other elements after dissolving the powder particles in a mixed acid. A triple determination method was used for each analyzing method and all powders. For that reason, a standard deviation of the detected average chemical composition is given in Table 2. The amount of carbon measured in PCA-2 was lower than expected. The addition of 0.5 wt. % of stearic acid should have given 0.38 wt. % of carbon. The stearic acid also coats the milling balls and the milling vessel, which explains the reduced carbon content in PCA-2. However, due to the abundance of carbon in PCA-2 the results of the experiments are not significantly affected by the lower amount of carbon.

2.1. Microscopy

Powder particles embedded in resin and subsequently polished were studied by scanning electron microscopy (SEM). Grinding and polishing were carried out with a series of progressively finer grained (from 320 to 1200 grit) SiC polishing papers. After that, a final polish using a diamond polishing suspension of 1 μm was performed. The sample was cleaned with isopropanol and a thin layer of gold was deposited on the polished surface to decrease electrical charging of the resin while recording EDX mappings.

The measurements were carried out using a Zeiss Merlin field-emission gun SEM with GEMINI II electron optics and an acceleration voltage of 30 keV. The elemental analysis was performed using energy dispersive x-ray (EDX) spectroscopy. ZAF correction was applied to all measurements. The magnification was chosen with respect to the powder particle size.

Two preparation methods for powder samples for transmission electron microscopy (TEM) have been used:

- Non-heat treated powder particles were embedded in resin. Focused ion beam preparation of individual powder particles was performed to obtain a TEM lamella. To remove the generated FIB damage on the surface of the lamella a flash polishing for 200 ms with a solution of 20% H_2SO_4 and 80% CH_3OH was performed.
- Heat treated powder particle of PCA-2 were pressed with a uniaxial pressure of 1000 MPa at 700 °C for one hour and afterward cooled down to room temperature in a vacuum environment. The discs with a thickness of around 1 mm were ground and polished to a thickness of around 200 μm. For the last step, a diamond polishing suspension of 1 μm was used. Afterward, electro-polishing in a TENUPOL V device by Struers with a mixture of 20% H_2SO_4 and 80% CH_3OH as an electrolyte was conducted at 20 °C. In the end, the samples were cleaned with an argon ion beam using a Precise Ion Polishing System (PIPS).

TEM studies were carried out using an FEI Tecnai 20 FEG analytical microscope with an accelerating voltage of 200 kV applying high-angle annular dark-field imaging (HAADF) technique in scanning TEM (STEM) mode for EDX analysis.

2.2. X-ray absorption spectroscopy

The XAS experiments were performed on the bending-magnet XAFS beamline at ELETTRA synchrotron (Trieste, Italy) [16]. The X-ray radiation was monochromatized by a 40% detuned Si(111) double crystal monochromator for the Ti K-edge (4966 eV), and without detuning for the Y K-edge (17,038 eV). The intensities of the incident and transmitted beams were measured by two ionization chambers filled with argon and krypton gasses. X-rays emitted by the sample were measured by a Si drift fluorescence detector.

For XAS measurements, ODS steel powders were sealed in quartz glass ampoules with outer and inner diameters of 6 and 4 mm, respectively. For the examination of powders in the mechanically alloyed state, approximately 1 g of each powder was placed in the quartz glass ampoules under argon atmosphere. More powder was used for heat treated samples to reduce the effect of oxidation while heating with residual oxygen. After filling, the ampoules were vacuum sealed without oxidizing the powder.

The quartz glass ampoules were mounted consecutively on a sample holder and were measured in fluorescence mode at the Y K-edge. For measurements performed at the Ti K-edge, the ampoules were opened and the powder was placed in Kapton tape because glass absorbed almost all of the signal. Yttrium (GoodFellow, 99.9%, thickness 0.025 mm) and titanium (GoodFellow, 99.6 + %, thickness 0.004 mm) foils were used for energy scale calibration and as references. In addition, a set of reference compounds was measured. We used commercial microcrystalline Ti_2O_3 (Aldrich, 99.9%), anatase TiO_2 (Aldrich, 99.8%) and cubic c-Y_2O_3 (Aldrich, 99.99%). Nanosized Y_2O_3 (nano-Y_2O_3,

Table 2
Determined chemical composition of used and produced powders in wt. %.

Powder	Fe	Cr	Ni	W	Mn	Ti	V	Y	O	C
PCA-0	Bal.	13.1	–	1.95	0.4	0.3	0.19	–	0.05	0.008
PCA-1	79.8	17.7	–	1.69	0.39	0.21	0.19	0.23	0.2	0.03
PCA-2[a]	67.3	16.31	14.10	1.51	0.36	0.16	0.16	0.18	0.13	0.3[b]
Fe_3Y	67.0	–	–	–	–	–	–	32.6	0.30	0.1
Cr	–	Bal.	–	–	–	–	–	–	0.93	0.156
Ni	–	–	Bal.	–	–	–	–	–	0.19	0.008
Std. Dev.	0.8	0.2	0.3	0.03	0.03	0.005	0.005	0.005	0.002	0.04

[a] 0.5 wt. % stearic acid is used as a PCA.
[b] Calculated value of carbon after adding a PCA is 0.38.

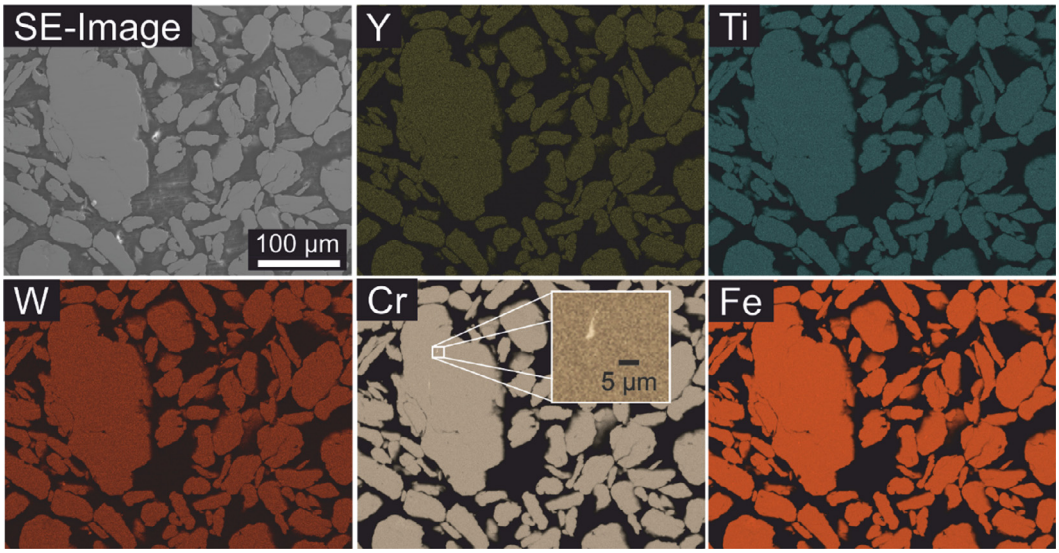

Fig. 1. SEM images of PCA-1 powder after 40 h of mechanical alloying. The magnified area shows an enrichment of chromium with a size of 6 µm.

3–4 nm) was synthesized using the extraction-pyrolytic method [17], and the crystallites size was determined by the Rietveld method. Microcrystalline Y_2TiO_5 and $Y_2Ti_2O_7$ were the same reference samples as used in [18]. The phase composition of reference samples was confirmed by X-ray powder diffraction measurements.

The obtained X-ray absorption spectra were processed using the Demeter [19] and EDA [20] software packages, using a conventional procedure [21] to extract the X-ray absorption near-edge structure (XANES) and the extended X-ray absorption fine structure (EXAFS).

3. Results and discussion

The two-step mechanical alloying process was evaluated using EDX method. Fig. 1 shows the ferritic ODS powder, PCA-1, after 40 h of milling. The elemental distributions of selected elements are depicted right next to a secondary electron (SE) image.

Even though chromium was gas-atomized together with all other elements in the prealloy, small enrichments with a lamellar shape and a size in the range from 1 to 5 µm were observed (see chromium distribution map). Other elements, like tungsten or titanium, which also tend to accumulate together with oxygen or carbon were not found in the form of clusters. The appearance of chromium clusters during the first mechanical alloying step can be connected to its abundance, and, thus, a sequestering together with carbon and/or oxygen is highly presumable due to the low Gibbs energy, even though no carbon or oxygen clusters have been found [22–24]. Therefore, it can be inferred that the small enrichments were caused by the addition of elemental chromium powder, which was not completely dissolved in the austenitic matrix. Nevertheless, the main focus of the first 40 h of milling is to homogeneously distribute and to dissolve the added yttrium in the ferritic matrix material. Recent studies have shown that 20 to 40 h (depending on the used milling parameters) are sufficient to achieve that [25,26]. No formation of yttrium-containing precipitates was observed.

The novel part is the second milling step, where ferritic ODS powder is blended and milled with nickel powder and stearic acid, which acts as a PCA. The microstructure of PCA-2 powder after the second milling step is represented in Fig. 2. This examination was conducted to determine the distribution of the added nickel powder after a mechanical alloying process of 12 h. In comparison with the Cr and Fe distribution images, regions lacking nickel, highlighted by arrows, can be identified. These areas were found to be two different types. The first are small regions located in relatively big powder particles, while the second type are small unalloyed powder particles of powder PCA-1. These regions or particles have a size of roughly 4–6 µm. In accordance with Suryanarayana [15], the milling process can be considered as finished after a lamellar spacing between the different powders (PCA-1 and Ni) of less than 1 µm is attained.

After 12 h of mechanical alloying, SEM EDX analyses showed that the defined lamellar spacing is not obtained for PCA-2. Usually, the powder is heated during the shaping process at temperatures of around 1000 °C, which enables diffusion processes to minimize the chemical gradients and support the formation of a uniform austenitic ODS steel. During the heating, the lamellar spacing will get reduced because of diffusion processes, which are strongly driven by a chemical gradient. Longer mechanical alloying times would also increase the number of impurities by wear and friction and a higher amount of stearic acid would be necessary to maintain a powder production yield of 100%. An optimized milling time needs to be defined in future research and was not part of this study. However, due to the mentioned processing route, a milling time of 12 h for a second milling step is sufficient to form austenitic steel during a subsequent heat treatment.

TEM images of powder PCA-2 provide deep insights into the microstructure. A HAADF STEM image of a lamella, which was cut out from one of the powder particles shown in Fig. 2, is imaged on the left-hand side in Fig. 3. Elemental distribution images of the red framed area are presented on the right-hand side and reveal the formation of titanium-rich precipitates with a size of 40–80 nm. To explain the formation of titanium-rich precipitates, it is important to emphasize that titanium was not added as an elemental powder and was originally present in PCA-0. Thereby, it can be inferred that a few titanium enrichments have formed clusters during the mechanical alloying process or that the precipitates formed during the powder production process (gas-atomization). In the first-mentioned case, titanium must have diffused during the mechanical alloying process, which only can be explained by locally heated zones in the powder, more vacancies and a lower activation energy due to the energy input by mechanical alloying [27,28]. The fact that titanium diffuses 7.6 times faster than iron in the austenitic matrix supports the theory of diffused titanium during the mechanical alloying process [29]. In the second-mentioned case, titanium was slightly oxidized during the gas-atomization and was not dissolved during the mechanical alloying process.

It was assumed that the formed precipitates are carbides or oxides due to a low Gibbs free energy of formation of those phases. However, no higher concentration of carbon was measured near titanium and only a slightly increased intensity of oxygen compared to the

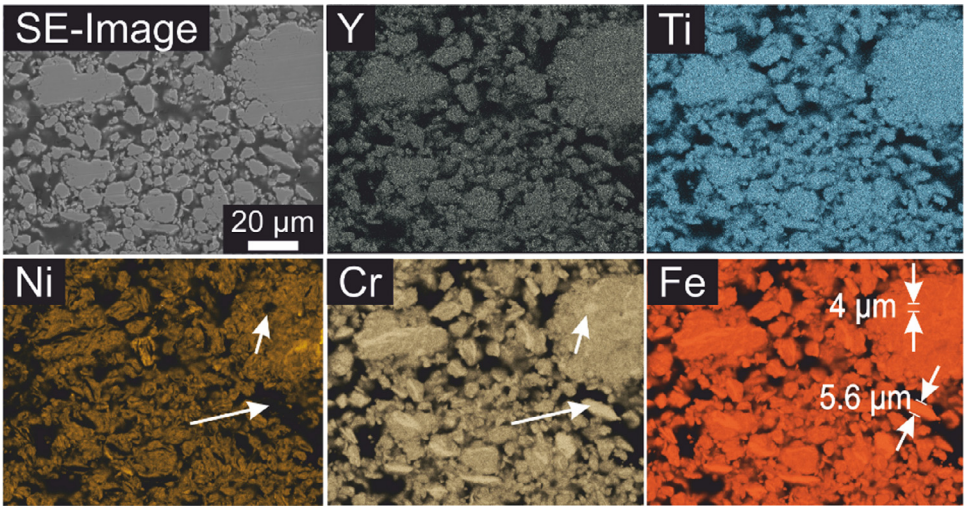

Fig. 2. Images of the elemental distribution in PCA-2 after 12 h of mechanical alloying. Arrows show unalloyed regions with a spatial extent of up to around 6 µm.

surrounding matrix material was detectable after separating the O-K_α and the Cr-L_α peak in the EDS spectra. This suggests that the titanium precipitates are partly oxidized. However, this analysis is not conclusive, as oxygen and carbon both present difficulties in detection via this method. This is because oxygen and carbon are both light elements and often are found as surface contaminations of the sample. Additionally, the attenuation length for the C-K_α x-ray energy was calculated to be approximately 50 nm inside the steel matrix. Assuming that the thickness of a TEM foil is less than 100 nm, this still leads to a strongly attenuated signal for carbon. This can lead to a low peak to background ratio, which may have happened in this case. Therefore, whether or not part of the titanium in the as-milled condition exists in metallic form cannot be confirmed. All other elements, except chromium, are homogeneously distributed. However, a part of the titanium must be dissolved into the matrix, which will lead to the formation of small Y-Ti-O rich precipitates after a heat treatment was applied. To investigate if the formation of smaller Y-Ti-O rich precipitates was triggered, powder samples were heat treated for 40 h at 1100 °C.

The microstructure of PCA-2 after the heat treatment is shown in Fig. 4 and reveals that a formation of rather big precipitates (dark in STEM image) with a diameter of around 100–200 nm occurred. Two of the particles were analyzed using an EDX line scan and are labeled “A” and “B” in the HAADF STEM and the oxygen distribution image. The graphs of the two line scans are shown below the TEM images. An increased amount of carbon in the bigger precipitates was identified, which can be explained by to the addition of the carbon-rich stearic acid as a PCA. These bigger precipitates were found to be free of yttrium. In terms of carbon, a rise in the number of counts from 200 to 300, and from 2100 to 2800, for precipitates A and B respectively, is measured. That means that the introduced carbon has formed and facilitated the formation of Cr(Ti)-O(C) clusters. Also, a correlation between Ti, Cr, and O without carbon was detected.

A comparison of the element distribution maps in Fig. 4 shows that Y precipitates smaller than 20 nm are well correlated with Ti. Due to this observation, the assumption that part of the titanium dissolves into the matrix material during mechanical alloying and forms precipitates together with yttrium during a subsequent annealing was confirmed.

To determine the extent of the influence of the carbon-containing PCA on the formation of the particles and their chemical composition, XAS methods were applied.

As can be seen in Fig. 5, yttrium is present mainly in the metallic state after mechanical alloying, and the most of yttrium is oxidized after heat treatment. This conclusion can be drawn from the comparison of the Y K-edge XANES for PCA-2 samples with reference materials Y foil and polycrystalline Y_2O_3 (c-Y_2O_3) Y_2TiO_5, $Y_2Ti_2O_7$, and nanosized Y_2O_3 (nano-Y_2O_3, 3–4 nm). Both pre-edge (feature A) and main edge (feature B) of the Y K-edge XANES of PCA-2 samples have the same energy as those of the references, suggesting a metallic state of yttrium after MA and its oxidation upon annealing at 1100 °C. The Y K-edge XANES spectrum of the PCA-2 sample after annealing has the same shape as to those of Y_2TiO_5 and nanosized Y_2O_3. At the same time, it misses post-edge double-peak feature C, characteristic for microcrystalline Y_2O_3, as well as the features D, characteristic for $Y_2Ti_2O_7$.

As mentioned, titanium also contributes to the increased mechanical properties at elevated temperatures by forming stable oxides, thus helping to boost the overall properties of the material [30]. However,

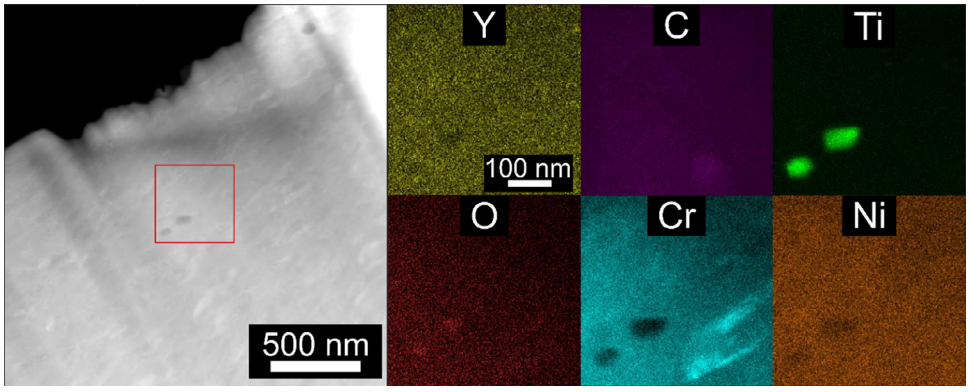

Fig. 3. HAADF STEM image of the microstructure of a powder particle of PCA-2 next to EDX images of selected elements.

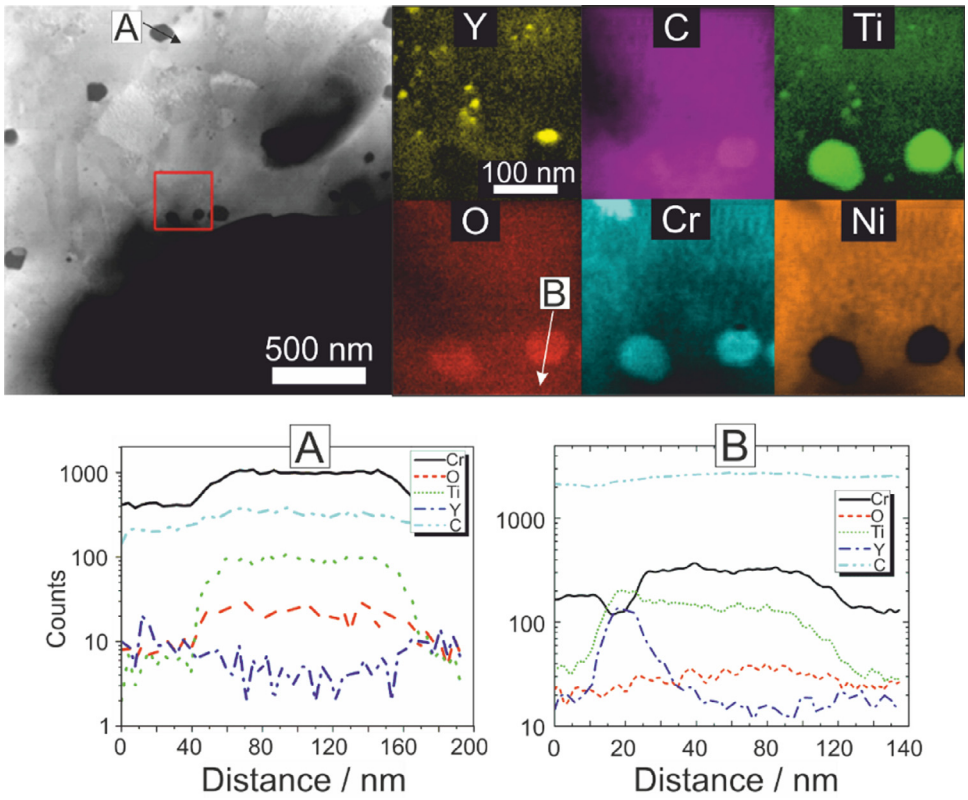

Fig. 4. Top left: HAADF STEM image of pressed powder of PCA-2 after 40 h of annealing at 1100 °C; top right: EDX images of the red section of selected elements; bottom: line scans "A" and "B" of big particles represented in the top images. (For interpretation of the references to color in this figure legend, the reader is referred to the web version of this article.)

the complex oxides containing both yttrium and titanium are the more favorable ones due to their low surface energy and an excellent lattice match between the austenite matrix and the nanoparticles [31,32]. This may help to mitigate the coarsening at high operating temperatures. The most mentioned and preferred stoichiometric composition is $Y_2Ti_2O_7$ [31,33–37]. But in the presence of carbon, titanium is also likely to form a stable carbide phase like the often found $M_{23}C_6$ phase [38–40]. For that reason, it was important to examine the behavior of titanium in as-milled and heat-treated condition when a carbon-rich PCA was added.

The Ti K-edge XANES and EXAFS spectra of PCA-2 samples before and after heat treatment are shown in Fig. 6. The spectra of untreated PCA-2 samples have the same features and absorption edge (except for the amplitude due to a nanosize) to that of TiO_2 (Anatase), indicating that titanium is mostly oxidized. This result is best seen in Fourier transforms of the EXAFS, where a very pronounced peak at 0.8–2.0 Å corresponds to the first coordination shell of Ti in oxides Ti-O. After annealing, the Ti K-edge spectrum of PCA-2 sample transforms to the one having the same XANES absorption edge values and the same features in XANES and EXAFS as Ti_2O_3, which corresponds well to TEM data where titanium is incorporated into the chromium and oxygen-rich precipitates. At the same time, this result does not exclude that a small fraction (around 10%) of Ti can be incorporated in Y-Ti-O oxides, but a strong correlation with Ti_2O_3 reference spectra indicates that the majority of Ti is in Ti^{3+} oxides.

4. Conclusions

Austenitic ODS steel has been investigated to reveal the impact of a carbon-containing PCA on the microstructure after milling and subsequent heat treatment. A novel two-step mechanical alloying process was applied and led to a powder production yield of 100%, which facilitates a scalable and reproducible process. We found that yttrium is well distributed after mechanical alloying and is only slightly oxidized. After annealing at 1100 °C yttrium and titanium form oxides. A majority of titanium is oxidized after mechanical alloying, however, bigger precipitates and enriched zones of titanium are also observable. After the annealing process titanium is present in a combination with yttrium

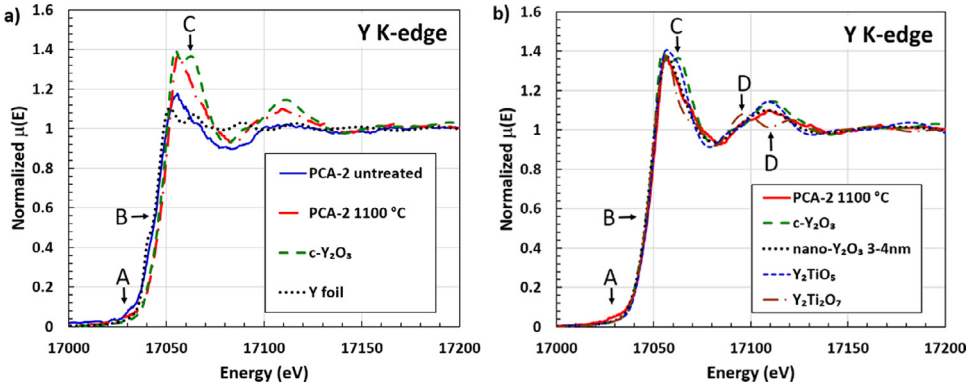

Fig. 5. Comparison of mechanically alloyed powder before and after a 40 h-long heat treatment at 1100 °C with the reference compounds.

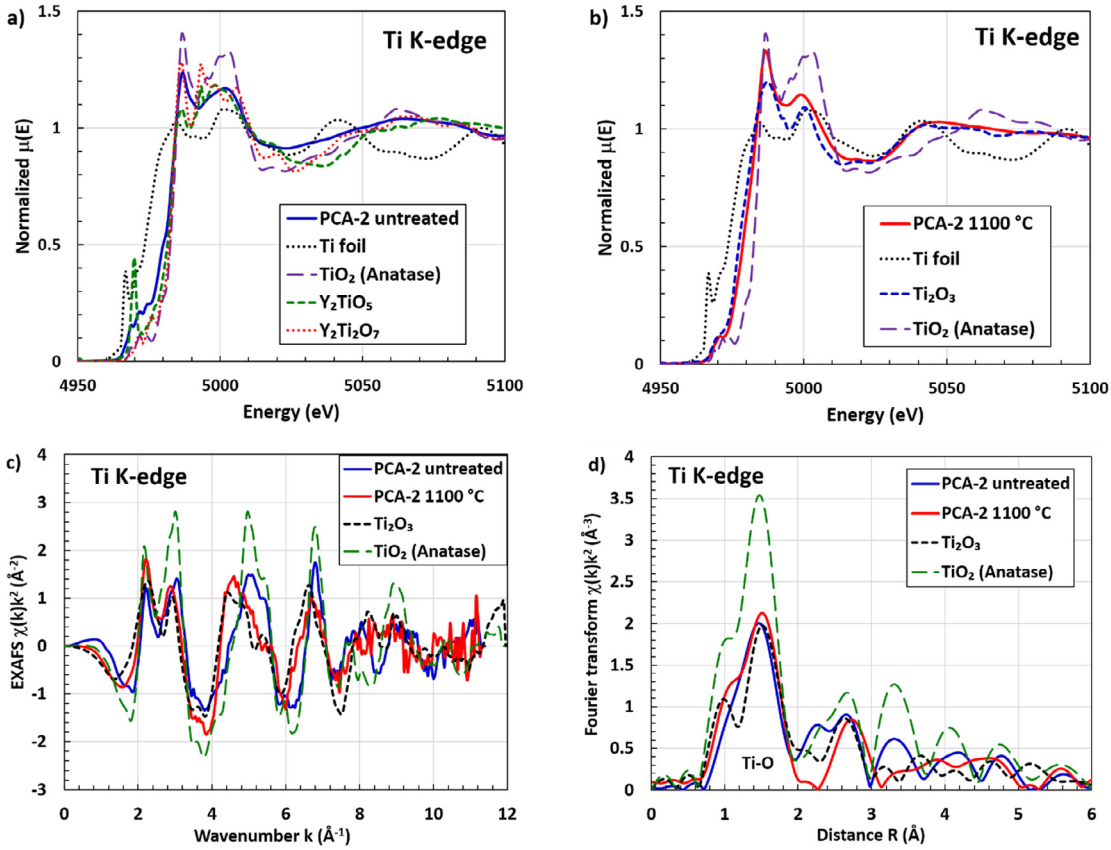

Fig. 6. Normalized Ti K-edge XANES spectra (a and b), EXAFS χ(k)k2 spectra (c) and their Fourier transforms (FTs) for PCA-2 (untreated and annealed at 1100 °C for 40 h) and reference compounds. Note that the distances and amplitudes in FTs do not correspond to the true crystallographic distances and to the shape of radial distribution function as they are distorted by photoelectron backscattering phase shift and amplitude.

forming smaller precipitates but also is traceable in bigger oxides and carbides next to chromium. It can be assumed that this leads to a reduced amount of titanium available for the formation of Ti-Y-O cluster. This indicates that a carbon-containing PCA has a negative influence on the formation of oxide nanoparticles in ODS steel. A more precise determination of its role in the processed material will be a subject of future studies.

Acknowledgment

The work of M. Parish and Rainer Ziegler is gratefully acknowledged. Thanks are also due to the team of the chemical laboratory at the KIT for performing the chemical analysis. The help of the beamline staff at ELETTRA (project 20140052) synchrotron radiation facility is acknowledged. We acknowledge support by Deutsche Forschungsgemeinschaft and Open Access Publishing Fund of Karlsruhe Institute of Technology.

Funding

This work has been carried out within the framework of the German Helmholtz Association and has received funding from the topic “Materials Research for the Future Energy Supply”.

Supplementary materials

Supplementary material associated with this article can be found, in the online version, at doi:10.1016/j.nme.2018.05.005.

References

[1] S.J. Zinkle, L.L. Snead, Designing radiation resistance in materials for fusion energy, Annu. Rev. Mater. Res. 44 (2014) 241–267, http://dx.doi.org/10.1146/annurev-matsci-070813-113627.
[2] S.J. Zinkle, A. Möslang, Evaluation of irradiation facility options for fusion materials research and development, Fusion Eng. Des. 88 (2013) 472–482, http://dx.doi.org/10.1016/j.fusengdes.2013.02.081.
[3] M.K. Miller, D.T. Hoelzer, E.A. Kenik, K.F. Russell, Stability of ferritic MA/ODS alloys at high temperatures, Intermetallics 13 (2005) 387–392, http://dx.doi.org/10.1016/j.intermet.2004.07.036.
[4] R. Lindau, A. Möslang, M. Schirra, P. Schlossmacher, M. Klimenkov, Mechanical and microstructural properties of a hipped RAFM ODS-steel, J. Nucl. Mater. 307–311 (2002) 769–772, http://dx.doi.org/10.1016/S0022-3115(02)01045-0.
[5] S.J. Zinkle, A. Möslang, T. Muroga, H. Tanigawa, Multimodal options for materials research to advance the basis for fusion energy in the ITER era, Nucl. Fusion 53 (2013) 104024, , http://dx.doi.org/10.1088/0029-5515/53/10/104024.
[6] R.L. Klueh, A.T. Nelson, Ferritic/martensitic steels for next-generation reactors, J. Nucl. Mater. 371 (2007) 37–52, http://dx.doi.org/10.1016/j.jnucmat.2007.05.005.
[7] R.L. Klueh, J.P. Shingledecker, R.W. Swindeman, D.T. Hoelzer, Oxide dispersion-strengthened steels: a comparison of some commercial and experimental alloys, J. Nucl. Mater. 341 (2005) 103–114, http://dx.doi.org/10.1016/j.jnucmat.2005.01.017.
[8] K. Ehrlich, S. Kelzenberg, H.D. Rahrig, L. Schafer, M. Schirra, The development of ferritic-martensitic steels with reduced long-term activation, J. Nucl. Mater. 212–215 (1994) 678–683.
[9] P. Susila, D. Sturm, M. Heilmaier, B.S. Murty, V. Subramanya Sarma, Microstructural studies on nanocrystalline oxide dispersion strengthened austenitic (Fe-18Cr-8Ni-2W-0.25\ce{Y_2O_3}) alloy synthesized by high energy ball milling and vacuum hot pressing, J. Mater. Sci. 45 (2010) 4858–4865, http://dx.doi.org/10.1007/s10853-010-4264-3.
[10] H. Oka, M. Watanabe, H. Kinoshita, T. Shibayama, N. Hashimoto, S. Ohnuki, S. Yamashita, S. Ohtsuka, In situ observation of damage structure in ODS austenitic steel during electron irradiation, J. Nucl. Mater. 417 (2011) 279–282, http://dx.doi.org/10.1016/j.jnucmat.2010.12.156.
[11] S.F. Li, Z.J. Zhou, L.F. Zhang, L.W. Zhang, H.L. Hu, M. Wang, G.M. Zhang, Corrosion behavior of a 304-oxide dispersion strengthened austenitic stainless steel in supercritical water, Mater. Corros. (2015), http://dx.doi.org/10.1002/maco.201508359 n/a-n/a.

[12] Y. Miao, K. Mo, G. Zhang, B. Cui, W.Y. Chen, V. Mccreary, D. Gross, I.M. Robertson, J.F. Stubbins, Development of austenitic ODS strengthened alloys for very high temperature applications, (n.d.) 1000.
[13] K. Suresh, M. Nagini, R. Vijay, M. Ramakrishna, R.C. Gundakaram, A.V. Reddy, G. Sundararajan, Microstructural studies of oxide dispersion strengthened austenitic steels, Mater. Des. 110 (2016) 519–525, http://dx.doi.org/10.1016/j.matdes.2016.08.020.
[14] T. Gräning, M. Rieth, J. Hoffmann, A. Möslang, Production, microstructure and mechanical properties of two different austenitic ODS steels, J. Nucl. Mater. 487 (2017) 348–361, http://dx.doi.org/10.1016/j.jnucmat.2017.02.034.
[15] C. Suryanarayana, Mechanical alloying and milling, Prog. Mater. Sci. 46 (2001) 1–184, http://dx.doi.org/10.1016/S0079-6425(99)00010-9.
[16] A. Di Cicco, G. Aquilanti, M. Minicucci, E. Principi, N. Novello, A. Cognigni, L. Olivi, Novel XAFS capabilities at ELETTRA synchrotron light source, J. Phys. Conf. Ser. 190 (2009) 12043, http://dx.doi.org/10.1088/1742-6596/190/1/012043.
[17] A.I. Khol'kin, T.N. Patrusheva, The extraction-pyrolytic method is 25 years old: results and prospects, Theor. Found. Chem. Eng. 50 (2016) 785–792, http://dx.doi.org/10.1134/S0040579516050109.
[18] G. Sattonnay, S. Cammelli, D. Menut, N. Sellami, C. Grygiel, I. Monnet, J.L. Béchade, J.P. Crocombette, A. Chartier, A. Soulié, R. Tétot, C. Legros, P. Simon, S. Miro, L. Thomé, Key role of the short-range order on the response of the titanate pyrochlore $Y_2Ti_2O_7$ to irradiation, Phys. Rev. B. 94 (2016) 1–8, http://dx.doi.org/10.1103/PhysRevB.94.224109.
[19] B. Ravel, M. Newville, ATHENA, ARTEMIS, HEPHAESTUS : data analysis for X-ray absorption spectroscopy using IFEFFIT, J. Synchrotron Radiat. 12 (2005) 537–541, http://dx.doi.org/10.1107/S0909049505012719.
[20] A. Kuzmin, EDA: EXAFS data analysis software package, Phys. B Condens. Matter. 208–209 (1995) 175–176, http://dx.doi.org/10.1016/0921-4526(94)00663-G.
[21] V.L. Aksenov, M.V. Kovalchuk, A.Y. Kuzmin, Y. Purans, S.I. Tyutyunnikov, Development of methods of EXAFS spectroscopy on synchrotron radiation beams: review, Crystallogr. Rep. 51 (2006) 908–935, http://dx.doi.org/10.1134/S1063774506060022.
[22] M. Small, E. Ryba, Calculation and evaluation of the gibbs energies of formation of Cr3C2, Cr7C3, and Cr23C6, Metall. Trans. A. 12 (1981) 1389–1396, http://dx.doi.org/10.1007/BF02643683.
[23] S.R. Shatynski, The thermochemistry of transition metal carbides, Oxid. Met. 13 (1979) 105–118, http://dx.doi.org/10.1007/BF00611975.
[24] C.V. Robino, Representation of mixed reactive gases on free energy (Ellingham–Richardson) diagrams, Metall. Mater. Trans. B. 27 (1996), http://dx.doi.org/10.1007/BF02915669 693–693.
[25] P. He, T. Liu, A. Möslang, R. Lindau, R. Ziegler, J. Hoffmann, P. Kurinskiy, L. Commin, P. Vladimirov, S. Nikitenko, M. Silveir, XAFS and TEM studies of the structural evolution of yttrium-enriched oxides in nanostructured ferritic alloys fabricated by a powder metallurgy process, Mater. Chem. Phys. 136 (2012) 990–998, http://dx.doi.org/10.1016/j.matchemphys.2012.08.038.
[26] M. Wang, Z. Zhou, H. Sun, H. Hu, S. Li, Microstructural observation and tensile properties of ODS-304 austeniticsteel, Mater. Sci. Eng. A. 559 (2013) 287–292, http://dx.doi.org/10.1016/j.msea.2012.08.099.
[27] B.B. Khina, G.F. Lovshenko, Modeling Enhanced Diffusion Mass Transfer in Metals during Mechanical Alloying, Sci. York, 2010.
[28] L. Lu, M.O. Lai, S. Zhang, Diffusion in mechanical alloying, J. Mater. Process. Technol. 67 (1997) 100–104, http://dx.doi.org/10.1016/S0924-0136(96)02826-9.
[29] T. Okita, W.G. Wolfer, F.a. Garner, N. Sekimura, Effects of titanium additions to austenitic ternary alloys on microstructural evolution and void swelling, Philos. Mag. 85 (2005) 2033–2048, http://dx.doi.org/10.1080/14786430412331331871.
[30] T.K. Kim, C.S. Bae, D. Kim, J. Jang, S.H. Kim, C.B. Lee, D. Hahn, Microstructural observation and tensile isotropy of an austenitic ODS steel, Nucl. Eng. Technol. 40 (2008) 305.
[31] X. Mao, K.H. Oh, S.H. Kang, T.K. Kim, J. Jang, On the coherency of Y2Ti2O7 particles with austenitic matrix of oxide dispersion strengthened steel, Acta Mater. 89 (2015) 141–152, http://dx.doi.org/10.1016/j.actamat.2015.01.060.
[32] Y. Miao, Advanced Characterizations of Austenitic Oxide Dispersion-Strengthened (Ods) Steels for High-Temperature Reactor Applications, University of Illinois at Urbana-Champaign, 2015.
[33] V. Badjeck, M.G. Walls, L. Chaffron, J. Malaplate, K. March, New insights into the chemical structure of $Y_2Ti_2O_7-\delta$ nanoparticles in oxide dispersion-strengthened steels designed for sodium fast reactors by electron energy-loss spectroscopy, J. Nucl. Mater. 456 (2015) 292–301, http://dx.doi.org/10.1016/j.jnucmat.2014.09.058.
[34] H. Sakasegawa, L. Chaffron, F. Legendre, L. Boulanger, T. Cozzika, M. Brocq, Y. de Carlan, Correlation between chemical composition and size of very small oxide particles in the MA957 ODS ferritic alloy, J. Nucl. Mater. 384 (2009) 115–118, http://dx.doi.org/10.1016/j.jnucmat.2008.11.001.
[35] J. Ribis, Y. De Carlan, Interfacial strained structure and orientation relationships of the nanosized oxide particles deduced from elasticity-driven morphology in oxide dispersion strengthened materials, Acta Mater. 60 (2012) 238–252, http://dx.doi.org/10.1016/j.actamat.2011.09.042.
[36] P.D. Edmondson, A. London, A. Xu, D.E.J. Armstrong, S.G. Roberts, Small-scale characterisation of irradiated nuclear materials: Part I – Microstructure, J. Nucl. Mater. 462 (2014) 369–373, http://dx.doi.org/10.1016/j.jnucmat.2014.11.067.
[37] M. Klimiankou, R. Lindau, A. Möslang, TEM characterization of structure and composition of nanosized ODS particles in reduced activation ferritic-martensitic steels, J. Nucl. Mater. 329–333 (2004) 347–351, http://dx.doi.org/10.1016/j.jnucmat.2004.04.083.
[38] V. de Castro, T. Leguey, A. Muñoz, M.A. Monge, R. Pareja, E.A. Marquis, S. Lozano-Perez, M.L. Jenkins, Microstructural characterization of Y2O3 ODS-Fe-Cr model alloys, J. Nucl. Mater. 386–388 (2009), http://dx.doi.org/10.1016/j.jnucmat.2008.12.136.
[39] A.L. Rouffié, J. Crépin, M. Sennour, B. Tanguy, A. Pineau, D. Hamon, P. Wident, S. Vincent, V. Garat, B. Fournier, Effect of the thermal ageing on the tensile and impact properties of a 18%Cr ODS ferritic steel, J. Nucl. Mater. 445 (2014) 37–42, http://dx.doi.org/10.1016/j.jnucmat.2013.10.030.
[40] R. Kasada, N. Toda, K. Yutani, H.S. Cho, H. Kishimoto, A. Kimura, Pre- and post-deformation microstructures of oxide dispersion strengthened ferritic steels, J. Nucl. Mater. 367–370 (A) (2007) 222–228, http://dx.doi.org/10.1016/j.jnucmat.2007.03.141.

Institute of Solid State Physics, University of Latvia as the Center of Excellence has received funding from the European Union's Horizon 2020 Framework Programme H2020-WIDESPREAD-01-2016-2017-TeamingPhase2 under grant agreement No. 739508, project CAMART²